Improving Gas Diffusion in Solid Oxide Cells Through Laser-Ablated Electrode Supports

S. Ganti-Agrawal[a], D. M. Cox[a], and S. A. Barnett[a]

[a] Department of Materials Science and Engineering, Northwestern University, Evanston, IL 60208, USA

In Ni-YSZ electrode-supported cells, gas diffusion through the electrode support layer can be a major limitation at high H_2 or H_2O utilization and high temperature. Conventionally, higher-porosity electrode supports are used to improve diffusion, but this diminishes the cell's structural integrity. Alternative fabrication methods like freeze-casting and 3D-printing allow for the creation of hierarchical structures with cutouts in the cell surface that improve gas diffusion, but these methods require redesigning processing procedures to obtain the desired materials properties. This work uses laser ablation to pattern cutouts into the electrode support after sintering, enabling a novel structure without redesigning the entire fabrication process. Current-voltage measurements of symmetric Ni-YSZ electrode-supported cells with one patterned and one un-patterned electrode demonstrate that laser-patterning improves limiting current density and effective diffusivity by as much as 30%. Mechanical testing of patterned and un-patterned cells demonstrates that patterned cells suffer relatively small reductions in fracture strength.

Introduction

Solid oxide cells (SOCs) can be an integral part of the future green hydrogen economy through the electrochemical production and consumption of hydrogen and hydrocarbon fuels (1,2). Reducing the cost of SOC operation relies on the ability to efficiently operate at high current densities with high reactant utilization to maximize the fuel produced or the electricity generated by each cell. The state-of-the-art SOC technology uses bilayer Ni-YSZ (yttria-stabilized zirconia) composite fuel electrodes: a fine fuel electrode functional layer (FEFL) to maximize reaction site density and a coarser thick Ni-YSZ fuel electrode support layer (FESL), which provides mechanical strength to the cell assembly (2). At high current densities, reactant utilizations and temperatures, the rate at which gases diffuse through the FESL becomes a performance-limiting factor; thus, improving SOC performance requires designing higher-diffusivity fuel electrode supports that still provide sufficient mechanical strength (3,4).

Previous work on improving FESL diffusivity has focused on optimizing conventional fabrication methods like tape-casting (4) or ceramic extrusion (5) to achieve higher support porosities. Rice determined that the strength of a cermet decreases exponentially with porosity – strength is proportional to e^{-bp}, where p is porosity and b is a fitting coefficient (6). As a result, conventional high porosity supports are fragile, which

impedes their adoption (4). In fact, Yu et al found that the flexural strength for Ni-YSZ cermets are in the range of 10 to 175 MPa - samples with a porosity near 25% had a strength of roughly 150 MPa, while samples with a 40% porosity had a strength close to 20 MPa (7). Novel fabrication methods like freeze-casting (8,9), 3D-printing (10), and phase-inversion (11-13) have been used to make supports with optimized pore geometries and achieve low tortuosity, but such methods require redesigning processing procedures and have not always yielded better properties than the baseline (10-12). On the other hand, laser-machining of the FESL offers a "drop-in" solution for improving support diffusivity. Laser-machining does not require modifications to the pre-existing casting and sintering processes and can be used to pattern prismatic cutouts into the support to reduce gas diffusion distances. Laser-machining has been previously used to pattern the electrode-electrolyte interface of SOCs (14-16), increasing active site density (15) and improving charge transport (16) across the electrolyte without inducing undesirable microstructural changes (14). Furthermore, Ceres Power has several patents on the use of laser-machining to create channels in metallic SOC interconnects (17,18), demonstrating the industrial viability of this manufacturing method. This work applies laser machining methods to pattern the cermet FESL, demonstrating that laser-patterning can offer improvements in limiting current density as large as 30%, while maintaining substantial mechanical strength.

Methods

Electrode supported symmetric cells were fabricated by tape-casting the FEFL, FESL, and the electrolyte. The FEFL and FESL were tape-cast using slurries with a 1:1 weight ratio of NiO (FuelCell Materials) and 8-YSZ (Tosoh) powders, while the electrolyte consisted of 8-YSZ with 1 mol% Fe_2O_3 (FuelCell Materials) added as a sintering aid. The FESL additionally used corn starch as a pore-forming agent. All slurries used Menhaden fish oil as a dispersant, polyvinyl butyral (B-95 grade) as a polymer binder, ethanol and xylene solvents, and a combination of benzyl butyl phthalate (TCW) and polyalkylene glycol (TCW) as plasticizers. The powders, solvents, and dispersants were ball-milled together for 24 hours, then the binders and plasticizers were added, and then the resulting mixture was ball-milled again for 24 hours. These electrode layers were then laminated together with 46.5 MPa of pressure at 80 C, punched into disks, and sintered at 1325 C for four hours, producing disks of 16 mm diameter and ~700 um thickness. This produced an average FESL thickness of 314 $\pm$ 11 μm (standard error), an FEFL thickness of ~25 μm, and an average electrolyte thickness of ~15 μm, as measured by a Wildscope Stereoscopic Optical Microscope.

After sintering, a LPKF Protolaser R laser cutter was used to cut the as-sintered cells into uniform 10 mm by 10 mm squares, as described by Cox (19), and then create four different cutout patterns within an 8 by 8 mm square on one side of the cell surface. These patterns were differentiated by their cutout and rib widths - P6-2, P6-3, and P6-4 used 600 μm cutout widths with 200 μm, 300 μm, and 400 μm rib widths respectively, while P3-1 used 300 μm cutout widths with 100 μm ribs. Cutout depths were measured using an Olympus Laser Confocal Microscope. Figure 1 shows an example of a patterned cell from P6-2, highlighting the cell layers and the cutout geometry.

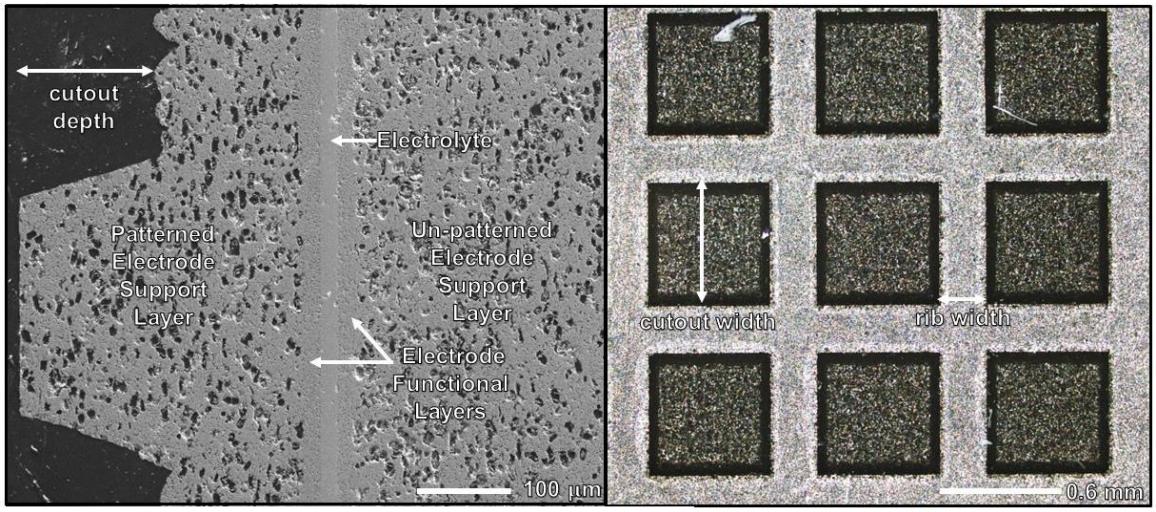

Figure 1. 100x SEM image of a cell cross-section (left) and 5x optical microscope image of the cell surface (right). The electrode supports, electrode functional layers and electrolyte layers are labeled, as well as the cutout depth, cutout width, and rib width.

TABLE I. Electrode Support Pattern Specifications.

Batch	Cutout Width (µm)	Rib Width (µm)	Cutout Area Fraction	Cutout Depth (µm)
6-2	600	200	0.36	140.4 ± 2.7
6-3	600	300	0.29	97.8 ± 5.5
6-4	600	400	0.23	161.6 ± 2.1
3-1	300	100	0.36	136.3 ± 26.3

Table I shows that there is substantial variability in the cutout depth, which is potentially caused by batch variability in FESL densities and cell curvature, which can affect the rate of laser ablation and how well the laser is focused on the sample surface – this range of cutout depths can affect the electrochemical performance, since cells with deeper cutouts could experience improved performance.

After laser-cutting, the cells were ramped up to 800 ˚C in a humidified mixture of 95% Ar and 5% H_2, then pre-reduced in humidified hydrogen (97% H_2, 3% H_2O) at 800 ˚C for 24 hours, and then ramped down to room temperature in the same dilute hydrogen mixture used for ramp-up. Cells were mounted, ramped up to 600 ˚C in the same dilute hydrogen mixture, and then tested in 97% H_2, 3% H_2O. In each cell test, between four to six cells were tested, divided evenly between control cells (un-patterned electrodes), and patterned cells (with one patterned and one un-patterned electrode). Cells were tested at 600 ˚C, 700 ˚C, and 800 ˚C using j-V sweeps (with a maximum applied voltage of 0.4 V in both bias directions) using a Squidstat Potentiostat (Admiral Instruments). The cell ohmic resistances were calculated from electrochemical impedance spectroscopy measurements at these temperatures, also using the Squidstat Potentiostat.

Cell porosity was determined through backscatter SEM characterization of a polished, epoxy-infiltrated cell. 15 mm × 5 mm × 0.7 mm rectangular cell samples were cast, sintered, laser-cut, and reduced as described before, to produce 3-point-bend test

specimens for the un-patterned and patterned case, which were tested in 3-point-bending using the RSA G2 Dynamic Mechanical Analyzer. The flexural stress at fracture was calculated from the following formula:

$$\sigma = \frac{3FL}{2bd^2}, \quad [1]$$

where F is the applied force, L is the span length of the 3-point bend setup (10 mm), b is the beam width (5 mm), and d is the beam thickness (~0.7 mm).

Results

Electrochemical Analysis

Figure 2 demonstrates how the j-V curve of a patterned cell differs from the j-V curve of an un-patterned cell. In a symmetric cell operating in an H_2/H_2O environment, the electrode under positive bias performs the hydrogen oxidation reaction:

$$H_2 + O^{2-} \rightarrow H_2O + 2e^- \quad [2]$$

while the electrode under negative bias performs the steam reduction reaction:

$$H_2O + 2e^- \rightarrow H_2 + O^{2-} \quad [3]$$

The symmetric cells were tested in a 97% H_2-3% H_2O environment, so the electrode performing the steam reduction reaction will be much more mass-transport-limited, due to the dilute steam concentration. Since un-patterned cells are fully symmetric, their electrodes perform steam reduction equally well, so switching the applied bias direction has a minimal effect on the j-V curve. However, the patterned cells have two distinct electrodes, so the j-V performance of the patterned cells depends on the direction of the applied bias. In Figure 2, we see that the sample un-patterned cell (from P6-3 at 600 ˚C) has roughly the same performance for both bias directions, whereas the sample patterned cell from the same batch has substantially improved j-V performance in the negative bias direction. In the testing setup used for this study, the negative bias direction corresponds to applying a negative bias to the patterned electrode, which results in the patterned electrode performing the steam reduction reaction. Thus, we see that the patterned electrode enables higher current densities than the un-patterned electrode.

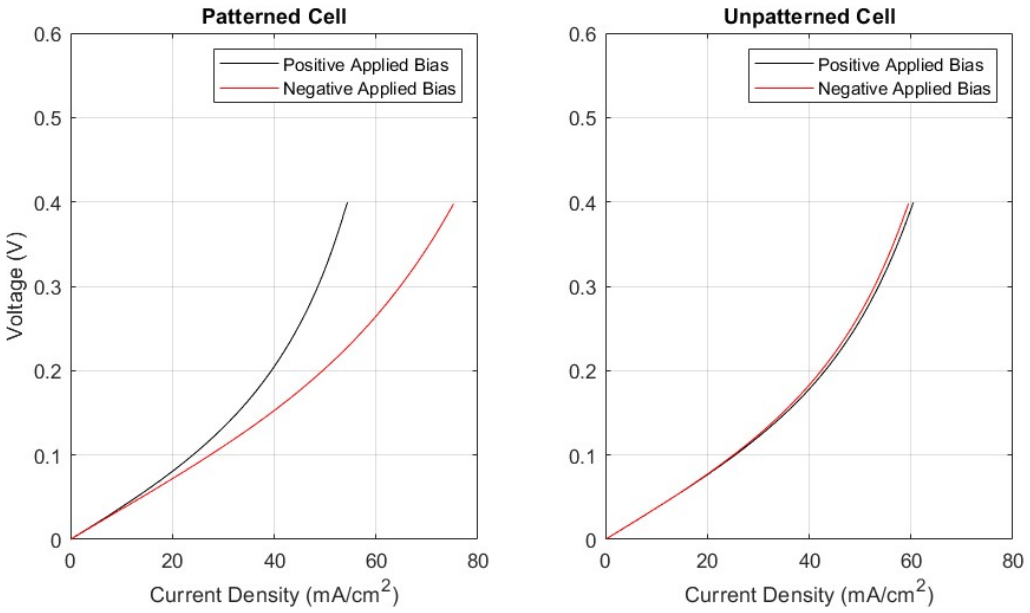

Figure 2. Comparison of the j-V performance for a patterned cell (left) and an un-patterned cell (right), using sample cells from P6-3, measured at 600 ˚C.

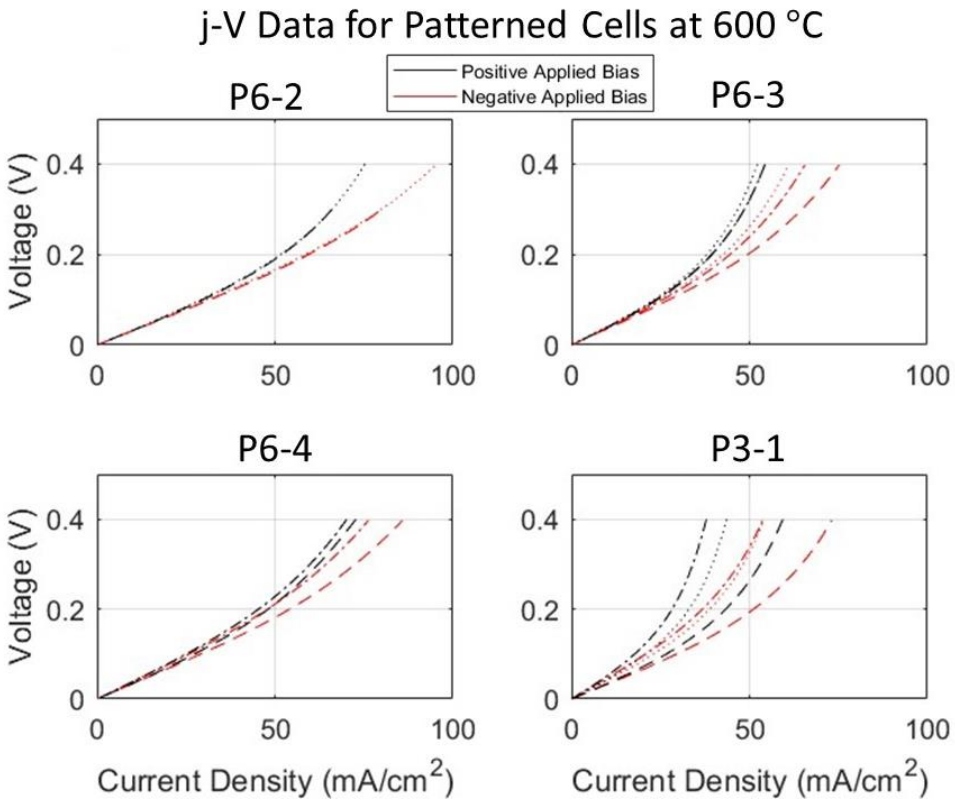

Figure 3. j-V performance in both bias directions for all patterned cells at 600 ˚C, for P6-2 (top-left), P6-3 (top-right), P6-4 (bottom-left), and P3-1 (bottom-right).

Figure 3 shows the j-V performance in both bias directions for all the batches at 600 ˚C. In all cases, there is an increase in the cell's current density when under negative

applied bias, which corresponds to the patterned electrode conducting the rate-limiting steam reduction reaction. Furthermore, the increase in current density appears to be the smallest for P6-4, and the largest for P6-2. This could be the result of large rib widths in P6-4 impeding in-plane gas diffusivity through the ribs, resulting in unequal gas distribution throughout the electrode functional layer, limiting performance improvements. Assuming that the reaction resistance is approximately constant, the j-V data was fit to the following expression, in terms of the limiting current densities for the two biasing directions:

$$V = jR_{\Omega} + Aln\left(\frac{j_{lim+}}{j_{lim+}-j}\right) + Bln\left(\frac{j_{lim-}}{j_{lim-}-j}\right) \quad [4]$$

where R_{Ω} is the cell's ohmic resistance (calculated from EIS measurements), j_{lim+} and j_{lim-} are the limiting current densities in the two bias directions; and A and B are temperature- and reaction-dependent coefficients fitted to the j-V data. Using the limiting current densities calculated from the curve-fitting, the effective diffusivities of H_2O in the patterned and un-patterned electrodes are calculated at 600 ˚C using the equation:

$$D_{H_2O}^{eff} = \frac{RTj_{lim}L_s}{2FP_{H_2O}^{\circ}} \quad [5]$$

where L_s is the thickness of the electrode and $P_{H_2O}^{\circ}$ is the pressure of H_2O in the system. Figure 4 shows the average $D_{H_2O}^{eff}$ in patterned and un-patterned electrodes at 600 ˚C.

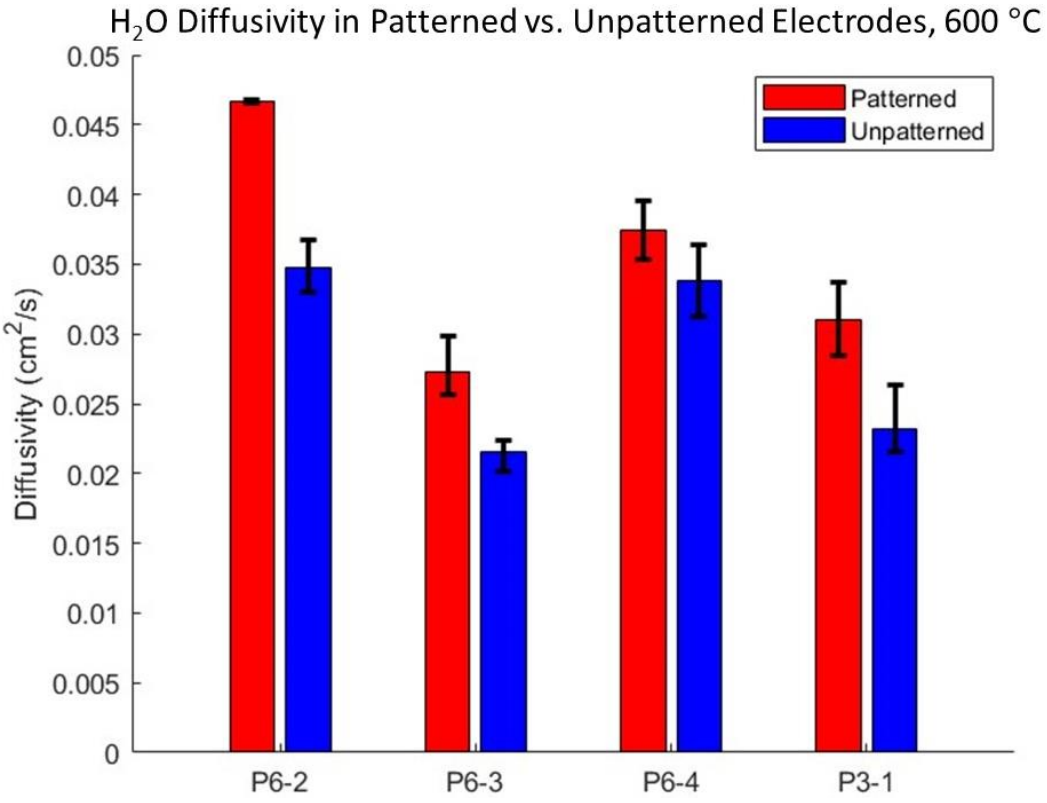

Figure 4. Diffusivity of H_2O in the patterned and un-patterned electrodes for P6-2, P6-3, P6-4, and P3-1, as determined from j-V data at 600 ˚C. Error bars represent the range of the averaged values.

Figure 4 demonstrates that the average diffusivity of patterned electrodes is substantially better, for P6-2, P6-3, and P3-1, where we get a 34%, 27%, and 34% increase in the average effective diffusivity respectively. This demonstrates that laser-patterning the electrode support can yield diffusional performance improvements of more than 30%. However, the diffusivity difference in P6-4, is within statistical margin of error. This matches the qualitative observations from Figure 3, which shows that batch 6-4 has the smallest current density increases.

Mechanical Analysis

The flexural strength of patterned and un-patterned symmetric cell samples was calculated from 3-point bend testing and plotted as a Weibull probability plot, as seen in Figure 5. All samples had dimensions of 5 mm by 15 mm, and the patterned samples had the P6-4 cutout pattern but with substantially deeper cutouts of 192 ± 3 μm (18% deeper) to ensure that the diffusional performance would be improved. For both patterned and un-patterned cells, the data closely fits the Weibull line of best-fit, indicating that the data can be represented with a Weibull distribution. From Figure 5, we see that the un-patterned cells have a higher flexural fracture strengths than the patterned cells, though there is some overlap in their Weibull probability distributions. The average flexural stress at fracture is 0.105 ± 0.011 MPa and 0.072 ± 0.004 MPa for un-patterned and patterned cells respectively, giving a 31% reduction in flexural strength.

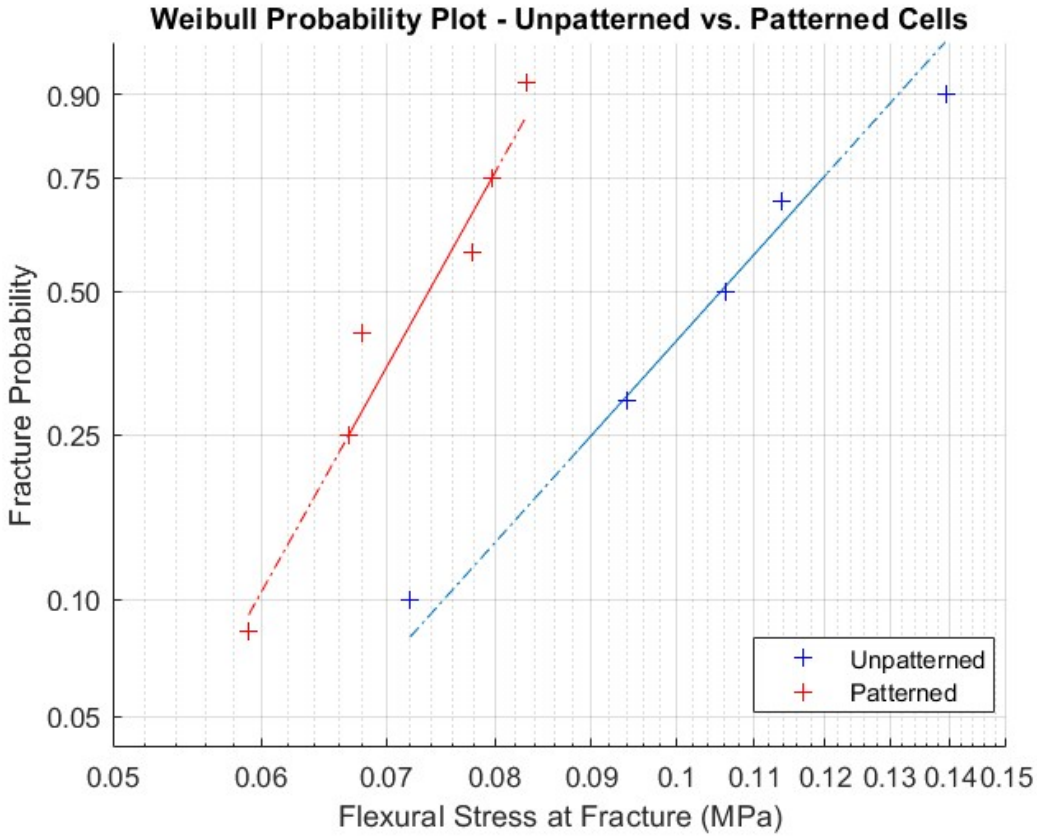

Figure 5. Weibull probability plot of the distribution of flexural stress at fracture for un-patterned and patterned cells tested with 3-point bending. For the patterned cells, the patterned electrode was in tension.

The symmetric cells porosity for this study was calculated to be 38%. Since the P6-4 cutout pattern (with extra-deep cutouts) is expected to yield a 20-30% current density increase, achieving the same performance improvement through a higher porosity support would require making cells with 43% to 45% porosity, based on the Bruggeman relation for diffusivity and porosity:

$$D_{eff} = \epsilon^{1.5} D \quad [6]$$

where D is the diffusivity of the material, D_{eff} is the effective diffusivity of the material, and ϵ is porosity (20). Based on Yu et al's findings, going from a porosity of 38% to a porosity of 43-45% could result in as much as a three-fold reduction in the cell's flexural strength (7). On the other hand, the patterned cell samples in this study have an average strength that is only 30% less than the unpatterned cells, which is much less of a drastic change. Thus, laser-patterned electrode supports can potentially provide the high performance of high-porosity electrode supports, while maintaining significantly higher durability. However, the strength values measured in this study are quite small – the flexural strengths of Ni-YSZ cermets measured by Yu et al are over two orders of magnitude larger (7). This deviation from the literature could be because the cell samples used in this study had an average thickness of 0.73 ± 0.01 mm, while the test specimens used by Yu et al were 2.5 mm thick (7) – the thinner samples could be more vulnerable to crack propagation and more vulnerable to the microstructural defects present. Furthermore, the test specimens used by Yu et al were isotropic, while the patterned and un-patterned cells in this study consist of distinct layers laminated together (the electrode support, electrode functional, and electrolyte layers), which could result in weak points along the interfaces. Thus, further investigation is necessary to identify whether the porosity-strength relationships identified in Yu et al's work are still valid for a multilayered SOC, as opposed to a homogenous Ni-YSZ cermet.

Conclusion

In this work, electrochemical, mechanical, and microstructural characterization of un-patterned and laser-patterned Ni-YSZ symmetric solid oxide cells was conducted. Laser-patterned electrodes consistently enabled higher current densities (near 30% higher for three of the cutout patterns tested) than un-patterned cells. Although laser-patterned cell samples have lower flexural strengths on average than the un-patterned cell samples tested, homogeneously increasing the electrode support porosity (e.g., by increasing higher pore-former content) results in much more significant strength decreases for the same level of performance improvement. Thus, laser-patterning solid oxide cell electrode supports offers a way to achieve large performance improvements at high current densities, without substantial compromises on cell durability.

Acknowledgments

The authors gratefully acknowledge financial support by the US National Science Foundation (NSF DMR- 1912530). This work made use of the NUFAB and EPIC facilities of Northwestern University's NUANCE Center, which has received support

from the SHyNE Resource (NSF ECCS-2025633), the IIN, and Northwestern's MRSEC program (NSF DMR-1720139). This work also made use of the Materials Characterization and Imaging Facility which receives support from the MRSEC Program (NSF DMR-1720139) of the Materials Research Center at Northwestern University.

References

1. A. Hauch, R. Küngas, P. Blennow, A. B. Hansen, J. B. Hansen, B. V. Mathiesen, and M. B. Mogensen. *Science* **2020,** *370*, eaba6118.
2. N. Mahato, A. Banerjee, A. Gupta, S. Omar, and K. Balani, *Prog. Mater. Sci.* **2015**, *72*, 141–337.
3. M. Ni, M. K. H Leung, and D. Y. C. Leung. *Energy Convers. Manag.* **2007**, *48*, 1525–1535.
4. B. K. Park, R. Scipioni, Q. Zhang D. Cox, P. W. Voorhees, and S. A. Barnett. *J. Mater. Chem. A* **2020**, *8*, 11687–11694.
5. H. Shimada, T. Suzuki, T. Yamaguchi, H. Sumi, K. Hamamoto, and Y. Fujishiro *J. Power Sources* **2016**, *302*, 53–60.
6. R. W. Rice, *J. Mater. Sci.* **1996**, *31*, 102–118.
7. J. H. Yu, G. W. Park, S. Lee, and S. K. Woo, *J. Power Sources* **2007**, *163*, 926–932.
8. Y. Du, N Hedayat, D. Panthi, H. Ilkhani, B. J. Emley, and T. Woodson. *Materialia* **2018**, *1*, 198–210.
9. C. Gaudillere and J. M. Serra *Bol. Soc. Esp. Cerámica Vidr.* **2016**, *55*, 45–54.
10. N. R. Geisendorfer and S. A. Barnett *ECS Meet. Abstr.* **2020**, *MA2020-01*, 1463.
11. D. Dong, X. Shao, K. Xie, X. Hu, G. Parkinson, and C. Z. Li, *Electrochem. Commun.* **2014**, *42*, 64–67.
12. D. Dong, X. Shao, X. Hu, K. Chen, K. Xie, L. Yu, Z. Ye, P. Yang, G. Parkinson, and C. Z. Li. *Int. J. Hydrog. Energy* **2016**, *41*, 19829–19835.
13. Y. Yang, F. Liu, X. Han, X. Wang, D. Dong, Y. Chen, P. Feng, M, Khan, S. Wang, and Y. Ling, *Appl. Energy* **2022**, *307*, 118222.
14. A. Larrea, D. Sola, M. A. Laguna-Bercero, J. I. Peña, R. I. Merino, and V. M. Orera, *J. Electrochem. Soc.* **2011**, *158*, B1193.
15. J. A. Cebollero, R. Lahoz, M. A. Laguna-Bercero, and A. Larrea, *J. Power Sources* **2017**, *360*, 336–344.
16. Y. Zhang, G. Cai, Y. Gu, L. Ge, Y. Zheng, H. Chen, and L Guo, *Energy Convers. Manag.* **2018**, *171*, 1030–1037.
17. B. C. H. Steele, A. Atkinson, J. A. Kilner, N. P. Brandon, and R. A. Rudkin, Patent US6794075B2, September 21, 2004.
18. R. Leah, M. Lankin, R. Pierce, and A. Bone, Patent CA2922744C, September 28, 2021.
19. D. M. Cox and S. A. Barnett, *J. Electrochem. Soc.* **2023**, *170*, 024514.
20. N. Zamel, X. Li, and J. Shen, *Energy Fuels* **2009**, *23*, 6070–6078.